

Wavelength-Selective Three-Dimensional Thermal Emitters via Imprint Lithography and Conformal Metallization

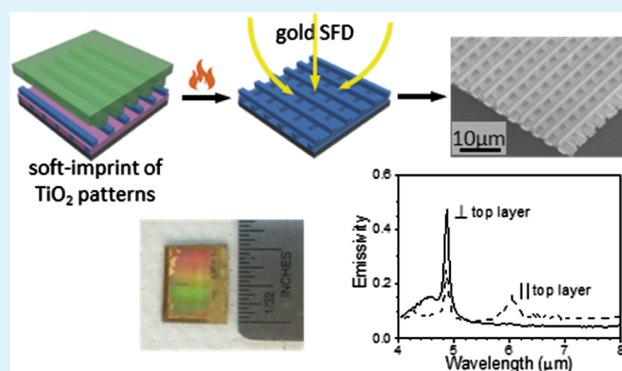
Shengkai Li,¹ Amir Kazemi-Moridani,[†] Yiliang Zhou, Irene R. Howell, Rohit Kothari,¹ Jae-Hwang Lee,[†] and James J. Watkins*

Department of Polymer Science and Engineering, University of Massachusetts Amherst, 120 Governors Drive, Amherst, Massachusetts 01003, United States

Supporting Information

ABSTRACT: Metallic photonic crystals (MPCs) exhibit wavelength-selective thermal emission enhancements and are promising thermal optical devices for various applications. Here, we report a scalable fabrication strategy for MPCs suitable for high-temperature applications. Well-defined double-layer titanium dioxide (TiO₂) woodpile structures are fabricated using a layer-by-layer soft-imprint method with TiO₂ nanoparticle ink dispersions, and the structures are subsequently coated with high purity, conformal gold films via reactive deposition from supercritical carbon dioxide. The resulting gold-coated woodpile structures are effective MPCs and exhibit emissivity enhancements at a selective wavelength. Gold coatings deposited using a cold-wall reactor are found to be smoother and result in a greater thermal emission enhancement compared to those deposited using a hot-wall reactor.

KEYWORDS: woodpile structure, imprint lithography, supercritical fluid deposition, conformal coating, wavelength-selective, thermal emitter



INTRODUCTION

Metallic photonic crystals (MPCs) are metallic structures with periodic nano-/microstructures. They enable specific light-matter interactions that give rise to unique optical properties nonexistent in traditional bulk materials, such as wide photonic band gaps^{1–3} and enhanced absorption at the band gap edges, leading to wavelength-selective thermal radiation enhancements.⁴ These properties make MPCs promising thermal optical devices for various applications including thermal photovoltaics,^{5–8} self-cooling devices,^{9–12} and chemical and biosensors.^{13,14}

The woodpile structure is a common structural choice for MPCs, as the structural dimensions can be easily tuned and multilayer structures can be fabricated through layer-by-layer strategies. The fabrication of these structures usually begins with the preparation of a polymeric or ceramic woodpile structure and is followed by metallization of the structure.

Common methods for the fabrication of the woodpile structure include direct laser writing^{15–18} and subtractive silicon wafer-based processes derived from semiconductor fabrication.^{4,7} These methods are limited by tedious fabrication procedures, slow speed, small area capability, and the need for expensive facilities and, in general, are not suitable for large-scale production. In comparison, soft-imprint lithography is an attractive technique to overcome these limitations, as the imprint procedure can be applied to a large area in a roll-to-roll

continuous process. This fabrication strategy is first illustrated by Lee et al.,¹⁹ with a technique called two-polymer microtransfer molding. Polymeric woodpile structures were fabricated by first carefully filling polydimethylsiloxane (PDMS) molds with UV-cross-linkable polymers and then transferring the polymerized material from the mold to the substrate. With this method, well-defined structures with up to 12 layers were obtained. The material of the structure, however, was limited to specific polymers, limiting further processing possibilities and imposing thermal limits on their use. More recently, Kothari et al.²⁰ reported the fabrication of woodpile structures with thermally stable ceramic materials, using a layer-by-layer imprint-planarize-imprint method. Well-defined TiO₂ woodpile structures up to 4 layers were fabricated from residue-layer-free soft imprinting of TiO₂ nanoparticle (NP) dispersions. Final calcination steps were needed to form a connected nanostructure, which also demonstrated the high thermal stability of the structure.

To metallize the woodpile structure, either a conformal metal coating or a complete metal backfilling is needed.²¹ Metal coating is more advantageous because it eliminates the need for etching away the template. Metal coatings on a ceramic

Received: November 6, 2017

Accepted: February 13, 2018

Published: February 13, 2018

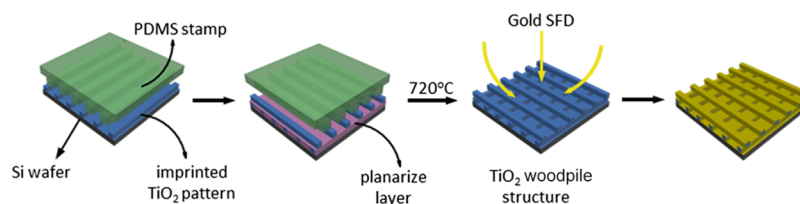


Figure 1. Schematic of the fabrication of gold-coated TiO₂ woodpile structures.

structural frame would also be more thermally stable and suitable for high-temperature applications compared to pure metal structures. A metal-coated structure would behave similarly to a pure metallic structure as long as the coating is thicker than its skin depth.²² Among different metals, gold is advantageous because it is highly resistive to oxidation, and its low bulk-phase emissivity provides a low baseline and high contrast to the emissivity enhancements.

Because of the woodpile's complex three-dimensional structure, achieving a conformal metal coating is especially challenging. As a result, physical vapor deposition methods such as evaporation and sputtering are not suitable due to their line-of-sight characteristics. Chemical deposition techniques are more suitable, and the use of electroless deposition^{17,23,24} and chemical vapor deposition (CVD)^{15,16} has been reported. Electroless deposition is a cheap and easy deposition method but is limited by the poor stability of reactant solutions and the difficulty in precisely controlling the film quality.²⁵ It also produces large amount of hazardous waste streams of which proper treatment can be costly. CVD is a more controllable process, but deposition on the surfaces of complex geometries suffers from the mass diffusion limitation due to the low vapor pressure of precursors. This leads to a low deposition rate at the inner surface and excess coating on the outer surface of the structure.¹⁵

In comparison, supercritical fluid deposition (SFD) is a promising technique to obtain conformal metal coatings on the complex surface of the woodpile structure. The technique uses supercritical carbon dioxide (scCO₂) as the reaction media, where CO₂ is heated and pressurized to above its critical temperature (31.1 °C) and critical pressure (7.39 MPa). scCO₂ possesses high diffusivity and low viscosity and dissolves metal–organic precursors and reducing agents at concentrations not accessible in vapor-phase depositions. The high solubility and high diffusivity alleviate the mass-transport limitations that typically exist in CVD processes and are especially suitable for conformal coating onto or within the high aspect ratio surfaces. This process also produces little hazardous waste, making it a much greener process than electroless deposition. Various kinds of metals have been deposited using this method,^{26–31} and highly conformal coatings have been reported on high aspect ratio trenches.^{32–35}

In this work, we demonstrate a new strategy for scalable fabrication of metallic woodpile structures. The previously reported layer-by-layer soft-imprint method²⁰ was adopted to fabricate large-area TiO₂ woodpile structures as a structural frame, and a high purity, conformal gold coating was deposited on the frame with the reported SFD method.³³ Double-layer structures are fabricated as they have been reported to exhibit the strongest and most wavelength-specific thermal emission enhancement with a conductive substrate surface and are reported to be similar to the four-layer woodpile structures without conductive substrate.³⁶ A comparison between metal

coatings using cold-wall and hot-wall reactors is discussed, as well as the thermal emission enhancements of the resulting structures.

EXPERIMENTAL SECTION

Materials. Norland optical adhesive 60 (NOA60) was purchased from Norland Products, Inc. Methanol (ACS grade) was purchased from Fisher Scientific. Propylene glycol monomethyl ether acetate (PGMEA, ReagentPlus grade) was purchased from Sigma-Aldrich. Dimethyl(acetylacetonate) gold(III) [(acac)Au(CH₃)₂] was purchased from Strem Chemicals and was used as received. Bone dry grade CO₂ (CD BD 300) and ultrahigh purity grade H₂ (HY UHP 300) were purchased from Airgas Inc. Silicon wafers of (100) orientation (p-type, boron dopant) were purchased from Nova Electronics, cut into small pieces, and treated with oxygen plasma for 2 min before use.

Titanium oxide (anatase, 20 wt %, 15 nm average particle size) NP dispersion in 1,2-propanediol was purchased from US Research Nanomaterials, Inc. It was further mixed with methanol at a solution-to-methanol weight ratio of 1.15, subjected to sonication for a few minutes, and filtered with 0.45 μm poly(tetrafluoroethylene) syringe filters before being used in soft imprinting.

PDMS stamps were prepared with a Sylgard 184 silicone elastomer kit purchased from Ellsworth. The grating pattern was replicated from SU-8 photoresist patterns on Si wafers developed after UV lithography. The dimensions of the gratings were 4 μm in periodicity, 2 μm in rod width, and 3 μm in rod height.

A schematic of the fabrication of the gold-coated woodpile structure is shown in Figure 1.

Woodpile Structure Fabrication. TiO₂ woodpile structures were fabricated on Si wafers using an imprint-planarize-imprint strategy that was reported previously for smaller dimensions.²⁰ Each layer of patterned TiO₂ was imprinted in a glove box with relative humidity regulated to less than 5%. The TiO₂ NP dispersion was spin-coated on the substrate at 1500 rpm for 4.5 min, and the PDMS stamp was gently placed onto the TiO₂ coating immediately afterward. The stamped substrate was then placed on a 50 °C hot plate for 6 h before the stamp was peeled off, and the imprinted TiO₂ pattern was exposed.

It is important to note that this imprinting time was chosen for convenience in this study to demonstrate feasibility. Recently, Li et al.³⁷ demonstrated the fabrication of TiO₂ woodpile structures using a similar ink and imprinting approach for use as high-performance lithium-ion battery anodes with an imprinting time of 5 min. In addition, Kothari et al.²⁰ demonstrated rapid imprinting of TiO₂ using an ink-containing TiO₂ NPs and a UV curable sol. In the case of imprinting with indium tin oxide NP inks, the imprinting time was reduced to 15 s.

A planarization step was needed on the imprinted TiO₂ pattern to form a planar surface to imprint the next layer. This was done with the UV-cross-linkable polymer NOA60 dissolved in PGMEA. The NOA60/PGMEA solution was spin-coated onto the imprinted TiO₂ pattern in two steps: first using a solution of 30 wt %, at 1000 rpm for 1.5 min, and then a solution of 20 wt %, at 2000 rpm for 1 min. This ensured a relatively flat surface with height variations less than 40 nm, as measured by a Verifire XL interferometer from Zygo. (Figure S1 in the Supporting Information). The surface was treated with O₂ plasma before each spin-coating step to improve the wetting of the surface, and the spin-coated film was exposed to UV curing for 10 min. The next layer of TiO₂ patterns was imprinted on the top of the planarized

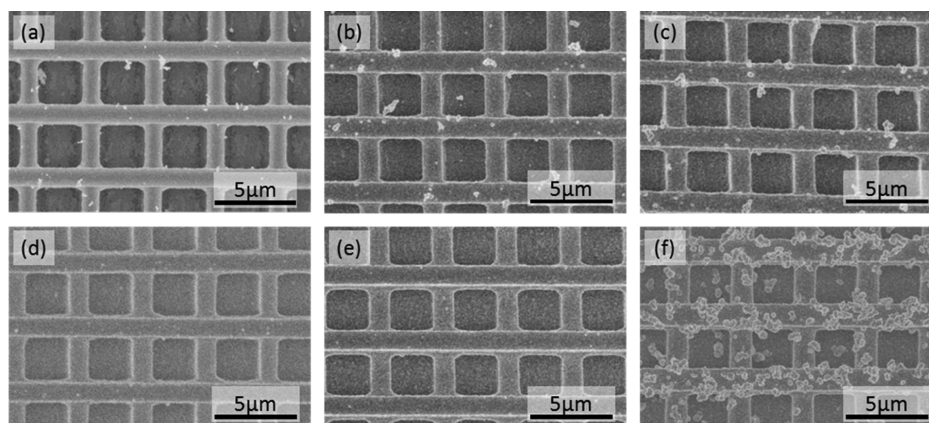


Figure 2. Top-down SEM images of gold-coated woodpile structures. (a–c) Samples coated using a hot-wall reactor, with precursor loadings of 0.018, 0.04, and 0.06 g, at 60 °C and (d–f) samples coated using a cold-wall reactor at 90, 120, and 150 °C.

layer perpendicular to the previous pattern without O₂ plasma treatment.

After these imprinting and planarization steps, the layer-by-layer patterned structures were calcined at 720 °C for 5 min and slowly cooled down to room temperature with 1 °C/min cooling rate to burn off the NOA60 and sinter the multilayer TiO₂ NPs into a woodpile structure. The shrinkage of TiO₂ structures upon calcination was measured and found to be approximately 25% for both horizontal and vertical directions.

Gold Deposition. Gold depositions were carried out either in a 30 mL hot-wall reactor or a 100 mL cold-wall reactor using setups and processes similar to those previously reported.³³

In the hot-wall reactor setup, a high-pressure stainless steel cylinder reactor was horizontally placed and wrapped with a heating band and a glass fiber insulator. A gas inlet was connected to one end of the cylinder, and the other end connected to an in-line filter and then to a carbon bed and a bubbler. A thermocouple rod was introduced from the outlet end to the center of the reactor volume to monitor the internal temperature. At equilibrium, the inner temperature reading from the thermal couple was within 5 °C of the set temperature of the outside wall.

In a typical deposition using the hot-wall reactor, a Teflon film was used to line the inner wall of the reactor, thereby preventing excessive deposition on the stainless steel inner wall. A magnetic stir bar was placed in the center of the tube, which was stirred by a rotating magnet outside the reactor. Substrates were placed on one side of the stir bar, and a known amount of (acac)Au(CH₃)₂ precursor was placed on the other side. The reactor was then connected to the inlets and outlets, purged with N₂ for 15 min, and then pressurized with CO₂ from a high-pressure ISCO Inc. model 500D syringe pump. The temperature of the outside wall was heated to 60 °C at the same time as the CO₂ introduction. The introduction of CO₂ was carefully monitored, so the pressure of the reactor was approximately 12.4 MPa when the temperature of the reaction volume was equilibrated at 60 °C. The equilibration was then kept for 30 min to dissolve the precursor into scCO₂.

After equilibration, the deposition reaction was started by introducing H₂ from a syringe pump similar to the one used for CO₂ introduction. The hydrogen introduction resulted in a pressure rise of about 2.0 MPa, which amounts to more than 100-fold stoichiometric excess in all cases. After 30 min reaction, the reactor was vented in less than 1 min, effectively stopping the reaction. The reactor was then repressurized and purged with scCO₂ at 60 °C and 12.4 MPa to extract any unreacted precursor and byproducts. The scCO₂ used for this cleaning step was more than three times the reaction volume.

In the cold-wall reactor setup, a cylindrical stainless steel reactor was placed vertically with a heating stage assembled at the bottom of the cylinder. An inlet for different gases and an outlet for purging and venting were connected to the top piece. The wall of the reactor was

heated by four cartridge heaters, and the heating stage was resistively heated using an embedded heating coil. As the pedestal temperature was much higher than that of the wall, the reaction proceeded selectively on the heated substrate.

In a typical deposition, substrates were placed onto the heating stage and a known amount of gold precursor was put in a small polyimide container and placed onto the stage. The reactor was then sealed, flushed with N₂, pressurized with CO₂, heated to 60 °C, and equilibrated for 30 min, and then H₂ was added, similar to the process for the hot-wall reactor. The stage heater was then set to higher deposition temperatures. The temperature of the heating stage rapidly increased, initiating the deposition. After 30 min reaction, the stage heater was turned off; the reactor was vented and then purged with scCO₂ at 60 °C and 12.4 MPa.

Characterization. Scanning electron microscopy (SEM) was carried out with a Magellan 400 XHR-SEM high-resolution scanning electron microscope from FEI. X-ray photoelectron spectroscopy (XPS) was carried out with Quantum 2000 scanning electron spectroscopy for the chemical analysis microprobe from Physical Electronics, Inc. The spot size was 0.5 mm × 0.5 mm. Atmospheric contaminants were removed from the sample by Ar⁺ sputtering. Raw XPS data were analyzed using MultiPak V6.1A software from Physical Electronics Inc. Surface height profiles were measured with a Verifire XL interferometer from Zygo. Atomic force microscopy (AFM) was carried out with SPM Dimension 3100 from Veeco, and data were analyzed with NanoScope V5.23 software from the same supplier.

The thermal radiation spectrum of the gold-coated TiO₂ structures was measured with a setup using a Fourier transform infrared (FTIR) spectrometer (Thermo Scientific, Nicolet 6700), similar to what was reported previously.³⁸ The detector was a MCT/A (HgCdTe or mercury cadmium telluride) detector and was cooled by liquid nitrogen. Samples were adhered to a hot plate and heated to temperatures between 180 and 220 °C. The temperature of the sample was monitored by measuring the emission of a thin PDMS film coated on the sample near the woodpile structure, using an infrared camera (FLIR, T450sc). Thermal radiation was measured at an incident angle of about 8° to avoid artifacts in the radiation spectrum, resulting from multiple reflections between the FTIR spectrometer and the highly reflective surface of the sample.³⁹ A linear polarizer was placed in the light path to study the polarization of the radiation enhancements. The measured radiation consisted of two parts: the radiation from the sample and the reflection from the surroundings. The reflection from the surroundings was constant for measurements at different temperatures, and the radiation from the sample can be expressed as a fraction of the blackbody radiation at the measurement temperatures. The ratio of radiation from the sample to the blackbody radiation is defined as emissivity and was assumed to be independent of temperature. Thus, comparing the radiation spectra at two different temperatures enables us to subtract the contribution of reflection and calculate emissivity spectra. The independence of emissivity from the

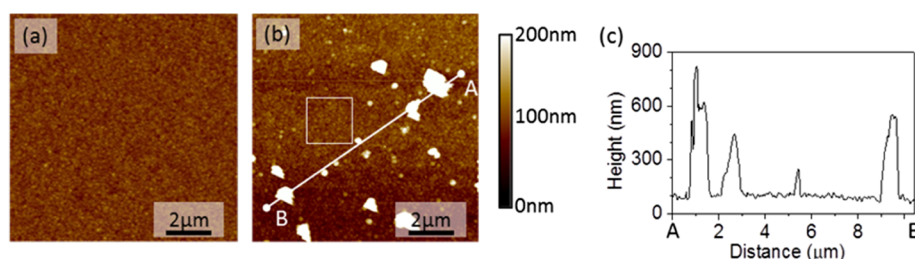


Figure 3. AFM images of gold-coated planar samples. (a) Coating obtained alongside the cold-wall sample; (b) coating obtained alongside the hot-wall sample; and (c) height profile of line AB in (b).

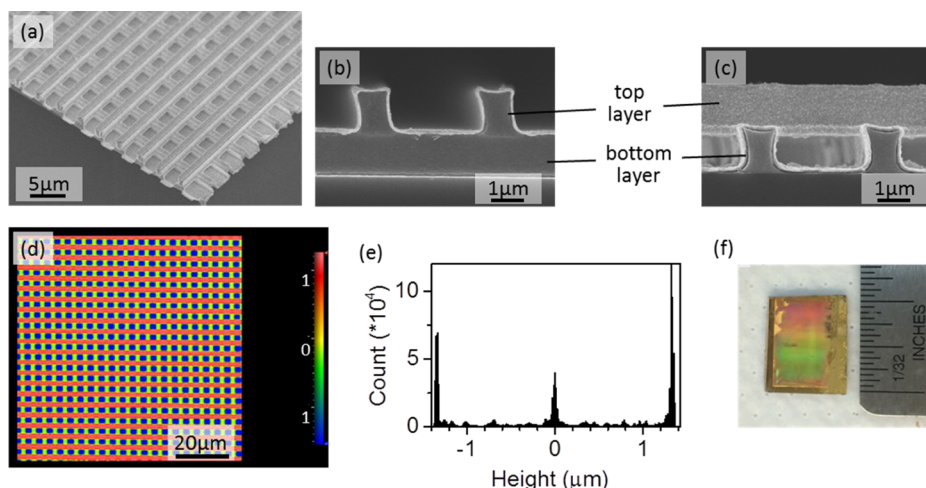


Figure 4. Cross-sectional SEM images, surface height profile, and photograph image of the gold-coated woodpile structure. (a) Cross-sectional SEM image at 45° angle; (b,c) cross-sectional images with bigger magnification at two different directions; (d,e) surface height profile (d) and its corresponding histogram (e); and (f) photograph image.

temperature was verified by collecting the radiation spectrum at a third temperature and comparing the spectrum with the prediction based on the calculated emissivity. The error limits of thermal emissivity measurements were less than 10%.

RESULTS AND DISCUSSION

Coverage of Gold Depositions. Gold coatings were deposited on fabricated double-layer TiO_2 woodpile structures with SFD using both cold-wall and hot-wall reactors. Depositions in the hot-wall reactor were carried out with precursor loadings of 0.018, 0.04, and 0.06 g, corresponding to initial precursor concentrations of 0.6, 1.3, and 2.0 g/L, respectively. Top-down SEM images of the structures after gold deposition are shown in Figure 2a–c. At 0.018 g loading, coverage of the gold coating was incomplete and significant exposure of the substrate could be found at the bottom of the woodpile structure, as indicated by the dark spots near the side of the squares. This can be seen more clearly in the SEM image with higher magnification in Figure S2a in the [Supporting Information](#). At larger precursor loadings, no such dark spots were found, showing full coverage of gold coatings. Depositions in the cold-wall reactor were carried out with a precursor loading of 0.06 g, corresponding to an initial precursor concentration of 0.6 g/L. In the cold-wall reactor, the substrate was heated to higher temperatures (90–150 °C) than the temperature used to dissolve the precursors. Here, gold coatings exhibited full coverage over the woodpile structure at all temperatures (Figure 2d–f).

The coverage of the gold coatings was also confirmed by XPS measurements. The XPS spectra can be found in Figure S2 in

the [Supporting Information](#). Besides confirming that the gold coverage agrees with what is observed in the SEM images, the spectra also show high purity of the gold coatings on the completely coated samples, without any carbon or oxygen contaminants.

As shown in Figure 2, additional particles were found on the surface of some gold coatings. These particles are pure gold particles as confirmed by XPS spectra. For coatings from the hot-wall reactor, particle existence was obvious even when the structure was not fully covered by gold coating. Samples fully covered by the gold film exhibited a similar particle density, with a particle size ranging from 0.1 to 0.7 μm in diameter. Samples deposited at 90 and 120 °C in the cold-wall reactor exhibited clean surfaces. Particles on these surfaces were very rare, with diameters less than 150 nm when present. However, deposition at 150 °C in the same reactor exhibited the largest amount of particles.

Particle formation can be explained by homogeneous nucleation that occurs in the scCO_2 phase. In the hot-wall reactor, the temperature distribution inside the reactor was uniform. In the cold-wall reactor, however, the temperature of the bulk scCO_2 phase was significantly lower than that of the substrate surface. At a deposition temperature of 120 °C or lower, this temperature difference was maintained at 18 °C or greater throughout the deposition process. A steep temperature gradient near the surface of the substrate is evident from the previous work in our group that employed both experimental and computational fluid dynamics to calculate full thermal profiles as well as fluid dynamics within cold-wall scCO_2 reactors.⁴⁰ This temperature gradient ensured the preference

of the gold deposition toward surface reaction, resulting in less particle formation. As the temperature of the substrate was increased further to 150 °C, the temperature of the bulk scCO_2 phase was also higher, reaching 105 °C at heat-transfer equilibrium. At this higher temperature, homogeneous nucleation near the substrate was also faster, possibly depleting reactants and hinders heterogeneous reaction. Therefore, particle formation was much more significant.

Typical double-layer samples with full coverage gold coatings obtained using both the cold-wall reactor and the hot-wall reactor were further characterized. For the cold-wall reactor, the sample with gold deposition at 120 °C was selected and will be referred to as the cold-wall sample; for the hot-wall reactor, the sample with gold deposition at 0.04 g precursor loading was selected and will be referred to as the hot-wall sample.

The coated surfaces of these samples were studied by AFM. Woodpile structures were not suitable for surface measurement by AFM because of the micrometer scale step changes in height. To simulate the gold-coated surface on a planar sample, TiO_2 NPs were spin-coated on to silicon wafers, calcinated at 720 °C, and deposited with gold alongside the woodpile structure samples. The AFM images of planar samples are shown in Figure 3. The coating from the cold-wall reactor at 120 °C (Figure 3a, coated alongside the cold-wall sample) shows a multi-grain morphology. The diameter of the grains was 90 ± 20 nm. It also exhibited a smooth surface, with a surface roughness of $r_a = 6.30$ nm and $\text{rms} = 8.00$ nm. In contrast, the coating obtained alongside the hot-wall sample exhibits additional surface particles over 400 nm high (Figure 3c). However, the area without the particles (area in the white box in Figure 3b) exhibited surface roughness similar to that of the cold-wall sample, ($r_a = 6.40$ nm, $\text{rms} = 8.07$ nm) as well as a similar grain size, with a diameter of 90 ± 30 nm.

Structural Characterizations. The structures of the samples were further characterized. Structure details of the cold-wall sample are shown in Figure 4, and similar structures of the hot-wall sample can be found in Figure S3 in the Supporting Information.

Figure 4a is the cross-sectional SEM image of the sample at a 45° angle, showing the conformal coating of gold all around the complex surface of the TiO_2 woodpile structure. Figure 4b,c is cross-sectional SEM images at greater magnifications, showing the near-rectangular shape of the gold-coated rods on each layer. The top and bottom of the rods were slightly wider than the middle, which was due to the solvent-assisted soft-imprinting process and has been reported in a similar process.⁴¹ The cross section of the top layer in Figure 4b leaned slightly to one side, resulting from the deformation of high aspect ratio features of the PDMS stamp in the imprinting process.

In Figure 4c, the gold coating on the side of the top layer clearly extends beneath the top surface of the bottom layer TiO_2 , indicating the existence of gold coating underneath the top layer TiO_2 lines. The absence of such gold coating in Figure 4b can be explained by the stripping of the gold film at the cracking point when preparing the sample for cross-sectional SEM characterization. The coverage of gold coating to the TiO_2 structure at the top left edge of Figure 4b, and the slight detachment of the coating from the TiO_2 frame seen in Figure 4c can be attributed to the same reason.

The coating thickness of the top layer measured from Figure 4b was 99 ± 8 nm, and that of the bottom layer measured from Figure 4c was 132 ± 11 nm. The coating on the top layer is somewhat thinner than that on the bottom layer. This

phenomenon cannot be explained by the mass-transport limitation in the deposition that usually occur in CVD processes, as the mass-transport limitation would result in a thicker coating on the top layer where mass transport was more facile. Rather, this should be attributed to the temperature difference in the deposition process. The top-layer TiO_2 surface, which is closer to the cooler supercritical CO_2 bulk fluid and farther from the hotter heating stage, would be cooler than the bottom layer. Therefore, deposition on the top layer would be slower, resulting in thinner coating.

The attribution of coating thickness difference to the temperature difference is further verified with a comparison to the hot-wall sample. The top and bottom layer coating thicknesses were measured to be 100 ± 9 and 106 ± 11 nm, respectively (Figure S3a,b). The thickness difference was within the standard deviations, and this thickness uniformity was due to the temperature uniformity associated with the hot-wall reactor.

Regardless of thickness variations, the coatings were much thicker than the skin depth of gold at IR wavelengths (~ 25 nm)²² and were therefore more than enough to ensure optical properties the same with those of pure gold structures. The coating thickness difference of the cold-wall sample was about 1.5 orders of magnitude smaller than the line width of the final structure. Therefore, the thickness difference was not expected to have a significant impact on the thermal emission property.

Figure 4d is the optical height profile obtained by interferometry, and a double-layer structure on the top of a planar surface is clearly evident. The dimension of the pattern was also measured. The periodicity and rod width were measured from the top-down SEM image (Figure 2d) and were 3.90 ± 0.05 and 1.21 ± 0.06 μm , respectively. The rod height was measured by the height difference of adjacent peaks in the height profile histogram (Figure 4e) and was 1.33 ± 0.02 μm . Measurements of the magnified cross-sectional images (Figure 4b,c) confirmed the structure dimensions.

Finally, Figure 4f shows the large area of the cold-wall sample. The size of the structure was about 7 mm \times 12 mm, with few defects on the structure. The size was only limited by the size of the PDMS stamp used in the imprinting and could easily be scaled by using larger stamps without significant variation of the fabrication process.

Thermal Emissivity Measurements. The thermal emission was measured for both the cold-wall sample and the hot-wall sample at polarizations both perpendicular and parallel to the top layer. Measurements were performed at 180 and 220 °C. Emissivities were calculated, and the emissivity spectra are shown in Figure 5. Comparing to the planar gold-coated samples that show constant low emissivity of less than 0.05 (Figure S4 in the Supporting Information), both samples exhibited a major emission enhancement peak at around 4.9 μm . This enhancement was detected at both polarizations as is shown more obviously in the spectra for the cold-wall sample (Figure 5a). This partially polarized emission enhancement is attributed to resonance modes at the photonic band edge and is expected to exist at the same wavelength within a wide detection angle.³⁸ This is further verified by the thermal emission measurement of the sample at other tilting angles (Figure S5 in the Supporting Information). Emission enhancements were also observed at approximately 4.5 and 6.0 μm . However, these enhancements were not only weaker but also highly polarized, indicating that they arose from the resonance modes of surface plasmon polaritons. The wavelength and

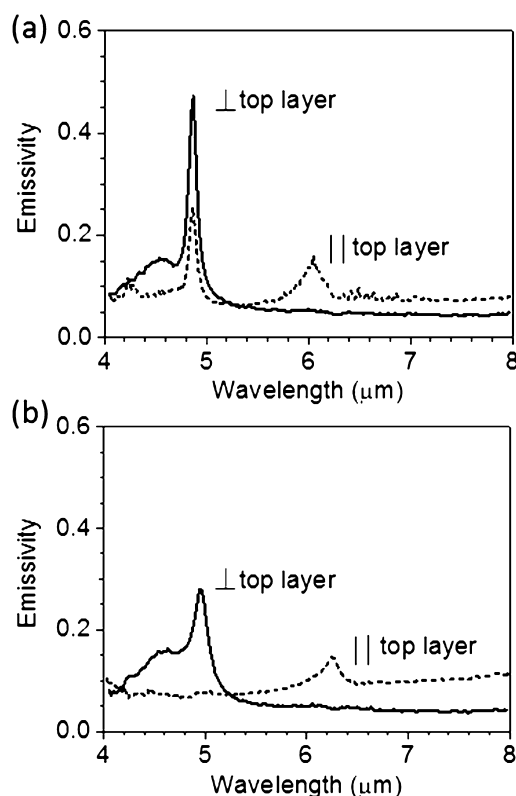


Figure 5. Emissivity spectra of gold-coated woodpile structures at polarizations perpendicular and parallel to the top layer (error limits less than 10%). (a) Cold-wall sample and (b) hot-wall sample.

intensity of these enhancements are therefore expected to vary strongly with the detection angle,^{42,43} so these enhancements would not be significant for wide-angle thermal emitter applications.

In comparison, the thermal enhancement of the hot-wall sample was significantly weaker than that of the cold-wall sample. This can be attributed to the particles that formed on the surface of the hot-wall sample, which results in more scattering loss.⁴⁴ Another possible reason for the weakened enhancement is that gold coatings prepared in the hot-wall reactor might have lower conductivities at high frequencies.⁴⁵

After the measurements, minor pinholes were found to have developed in gold coating (Figure S6 in the [Supporting Information](#)). However, the measured thermal emissivity spectrum over several hours of thermal treatment at 220 °C was essentially unchanged, with variations within the error limits. This result indicates that the pinholes do not affect the thermal emission, and the thermal stability of the fabricated structure was adequate for the thermal emission application.

CONCLUSIONS

We have demonstrated a scalable fabrication method for the gold-coated double-layer TiO₂ woodpile structures that are thermal emitters at mid-IR wavelengths. The well-defined TiO₂ woodpile structures were fabricated using an imprint-planarize-imprint technique with TiO₂ NP dispersion inks. Full coverage conformal gold coatings of high purity were deposited onto the woodpile structures using SFD. Gold films deposited in a cold-wall reactor were smoother compared to those deposited in a hot-wall reactor with no obvious particle formation on the coating surface. The resulting gold-coated structures exhibited

thermal emission enhancements at approximately 4.9 μm, with samples from the cold-wall reactor yielding stronger enhancement. This wavelength-selective enhancement is of great utility for thermal photovoltaics, self-cooling devices, and biochemical sensors, and the ceramic/metal hierarchical structure is promising for high thermal stability. This fabrication method combines the scalability of imprint technology with the fast and conformal metal coating of SFD to fabricate MPCs with high structural quality and is promising for scalable fabrication of such nano- and microstructured devices.

ASSOCIATED CONTENT

Supporting Information

The Supporting Information is available free of charge on the ACS Publications website at DOI: 10.1021/acsami.7b16902.

Height profiles of TiO₂ grating pattern after planarization steps, SEM image and XPS spectra of gold-coated woodpile structures, cross-sectional SEM images and surface height profile of the hot-wall sample, emissivity spectra of the planar sample gold-coated along with the cold-wall sample at two perpendicular polarizations, thermal emissivity spectra of the cold-wall sample measured at different tilting angles at polarizations parallel to the top-layer polarization, and SEM image of the cold-wall sample after thermal emission measurements (PDF)

AUTHOR INFORMATION

Corresponding Author

*E-mail: watkins@polysci.umass.edu.

ORCID

Shengkai Li: 0000-0001-6825-4398

Rohit Kothari: 0000-0002-0256-1632

Jae-Hwang Lee: 0000-0002-2546-1044

Present Address

[†]Department of Mechanical and Industrial Engineering, University of Massachusetts Amherst, Amherst, MA 01003, United States.

Notes

The authors declare no competing financial interest.

ACKNOWLEDGMENTS

This work was supported by the NSF Center for Hierarchical Manufacturing at the University of Massachusetts, Amherst (CMMI-1025020).

REFERENCES

- (1) Sigalas, M. M.; Chan, C. T.; Ho, K. M.; Soukoulis, C. M. Metallic Photonic Band-Gap Materials. *Phys. Rev. B: Condens. Matter Mater. Phys.* **1995**, *52*, 11744–11751.
- (2) Fan, S.; Villeneuve, P. R.; Joannopoulos, J. D. Large Omnidirectional Band Gaps in Metalodielectric Photonic Crystals. *Phys. Rev. B: Condens. Matter Mater. Phys.* **1996**, *54*, 11245–11251.
- (3) McIntosh, K. A.; Mahoney, L. J.; Molvar, K. M.; McMahon, O. B.; Verghese, S.; Rothschild, M.; Brown, E. R. Three-Dimensional Metalodielectric Photonic Crystals Exhibiting Resonant Infrared Stop Bands. *Appl. Phys. Lett.* **1997**, *70*, 2937–2939.
- (4) Lin, S. Y.; Fleming, J. G.; Li, Z. Y.; El-Kady, I.; Biswas, R.; Ho, K. M. Origin of Absorption Enhancement in a Tungsten, Three-Dimensional Photonic Crystal. *J. Opt. Soc. Am. B* **2003**, *20*, 1538–1541.

- (5) Lin, S. Y.; Moreno, J.; Fleming, J. G. Three-Dimensional Photonic-Crystal Emitter for Thermal Photovoltaic Power Generation. *Appl. Phys. Lett.* **2003**, *83*, 380–382.
- (6) Fleming, J. G.; Lin, S. Y.; El-Kady, I.; Biswas, R.; Ho, K. M. All-Metallic Three-Dimensional Photonic Crystals with a Large Infrared Bandgap. *Nature* **2002**, *417*, 52–55.
- (7) Lin, S.-Y.; Fleming, J. G.; El-Kady, I. Three-Dimensional Photonic-Crystal Emission through Thermal Excitation. *Opt. Lett.* **2003**, *28*, 1909–1911.
- (8) Lin, S.-Y.; Fleming, J. G.; El-Kady, I. Experimental Observation of Photonic-Crystal Emission Near a Photonic Band Edge. *Appl. Phys. Lett.* **2003**, *83*, 593–595.
- (9) Bartoli, B.; Catalanotti, S.; Coluzzi, B.; Cuomo, V.; Silvestrini, V.; Troise, G. Nocturnal and Diurnal Performances of Selective Radiators. *Appl. Energy* **1977**, *3*, 267–286.
- (10) Granqvist, C. G.; Hjortsberg, A. Radiative cooling to low temperatures: General Considerations and Application to Selectively Emitting SiO Films. *J. Appl. Phys.* **1981**, *52*, 4205–4220.
- (11) Granqvist, C. G.; Hjortsberg, A. Surfaces for Radiative Cooling: Silicon Monoxide Films on Aluminum. *Appl. Phys. Lett.* **1980**, *36*, 139–141.
- (12) Raman, A. P.; Anoma, M. A.; Zhu, L.; Rephaeli, E.; Fan, S. Passive Radiative Cooling below Ambient Air Temperature under Direct Sunlight. *Nature* **2014**, *515*, 540–544.
- (13) Seddon, A. B. A Prospective for New Mid-Infrared Medical Endoscopy Using Chalcogenide Glasses. *Int. J. Appl. Glass Sci.* **2011**, *2*, 177–191.
- (14) Ródenas, A.; Martín, G.; Arezki, B.; Psaila, N.; Jose, G.; Jha, A.; Labadie, L.; Kern, P.; Kar, A.; Thomson, R. Three-Dimensional Mid-Infrared Photonic Circuits in Chalcogenide Glass. *Opt. Lett.* **2012**, *37*, 392–394.
- (15) Nagpal, P.; Han, S. E.; Stein, A.; Norris, D. J. Efficient Low-Temperature Thermophotovoltaic Emitters from Metallic Photonic Crystals. *Nano Lett.* **2008**, *8*, 3238–3243.
- (16) Rill, M. S.; Plet, C.; Thiel, M.; Staude, I.; Von Freymann, G.; Linden, S.; Wegener, M. Photonic Metamaterials by Direct Laser Writing and Silver Chemical Vapour Deposition. *Nat. Mater.* **2008**, *7*, 543–546.
- (17) Terzaki, K.; Vasilantonakis, N.; Gaidukeviciute, A.; Reinhardt, C.; Fotakis, C.; Vamvakaki, M.; Farsari, M. 3D Conducting Nanostructures Fabricated Using Direct Laser Writing. *Opt. Mater. Express* **2011**, *1*, 586–597.
- (18) Hossain, M. M.; Gu, M. Broadband Optical Absorptions in Inversed Woodpile Metallic Photonic Crystals. *Opt. Mater. Express* **2012**, *2*, 996–1002.
- (19) Lee, J.-H.; Kim, C.-H.; Ho, K.-M.; Constant, K. Two-Polymer Microtransfer Molding for Highly Layered Microstructures. *Adv. Mater.* **2005**, *17*, 2481–2485.
- (20) Kothari, R.; Beaulieu, M. R.; Hendricks, N. R.; Li, S.; Watkins, J. J. Direct Patterning of Robust One-Dimensional, Two-Dimensional, and Three-Dimensional Crystalline Metal Oxide Nanostructures Using Imprint Lithography and Nanoparticle Dispersion Inks. *Chem. Mater.* **2017**, *29*, 3908–3918.
- (21) Hossain, M. M.; Gu, M. Fabrication Methods of 3D Periodic Metallic Nano/Microstructures for Photonics Applications. *Laser Photon. Rev.* **2014**, *8*, 233–249.
- (22) Biswas, R.; Zhou, D.; Puscasu, I.; Johnson, E.; Taylor, A.; Zhao, W. Sharp Thermal Emission and Absorption from Conformally Coated Metallic Photonic Crystal with Triangular Lattice. *Appl. Phys. Lett.* **2008**, *93*, 063307.
- (23) Zalkovskij, M.; Malureanu, R.; Andryeuskii, A.; Lavrinenko, A. V. Fabrication and Characterization of Woodpile Structures. In *SPIE Optics + Optoelectronics*; International Society for Optics and Photonics, 2011, 8070, 80700M-1-80700M-7.
- (24) Vasilantonakis, N.; Terzaki, K.; Sakellari, I.; Purlys, V.; Gray, D.; Soukoulis, C. M.; Vamvakaki, M.; Kafesaki, M.; Farsari, M. Three-Dimensional Metallic Photonic Crystals with Optical Bandgaps. *Adv. Mater.* **2012**, *24*, 1101–1105.
- (25) Antonello, A.; Jia, B.; He, Z.; Buso, D.; Perotto, G.; Brigo, L.; Brusatin, G.; Guglielmi, M.; Gu, M.; Martucci, A. Optimized Electroless Silver Coating for Optical and Plasmonic Applications. *Plasmonics* **2012**, *7*, 633–639.
- (26) Watkins, J. J.; Blackburn, J. M.; McCarthy, T. J. Chemical Fluid Deposition: Reactive Deposition of Platinum Metal from Carbon Dioxide Solution. *Chem. Mater.* **1999**, *11*, 213–215.
- (27) Long, D. P.; Blackburn, J. M.; Watkins, J. J. Chemical Fluid Deposition: a Hybrid Technique for Low-Temperature Metallization. *Adv. Mater.* **2000**, *12*, 913–915.
- (28) Blackburn, J. M.; Long, D. P.; Cabañas, A.; Watkins, J. J. Deposition of Conformal Copper and Nickel Films from Supercritical Carbon Dioxide. *Science* **2001**, *294*, 141–145.
- (29) Cabañas, A.; Shan, X.; Watkins, J. J. Alcohol-Assisted Deposition of Copper Films from Supercritical Carbon Dioxide. *Chem. Mater.* **2003**, *15*, 2910–2916.
- (30) Hünde, E. T.; Watkins, J. J. Reactive Deposition of Cobalt and Nickel Films from Their Metallocenes in Supercritical Carbon Dioxide Solution. *Chem. Mater.* **2004**, *16*, 498–503.
- (31) Kondoh, E. Deposition of Ru Thin Films from Supercritical Carbon Dioxide Fluids. *Jpn. J. Appl. Phys.* **2005**, *44*, 5799.
- (32) Blackburn, J. M.; Long, D. P.; Watkins, J. J. Reactive Deposition of Conformal Palladium Films from Supercritical Carbon Dioxide Solution. *Chem. Mater.* **2000**, *12*, 2625–2631.
- (33) Cabañas, A.; Long, D. P.; Watkins, J. J. Deposition of Gold Films and Nanostructures from Supercritical Carbon Dioxide. *Chem. Mater.* **2004**, *16*, 2028–2033.
- (34) O'Nei, A.; Watkins, J. J. Reactive Deposition of Conformal Ruthenium Films from Supercritical Carbon Dioxide. *Chem. Mater.* **2006**, *18*, 5652–5658.
- (35) Watanabe, M.; Takeuchi, Y.; Ueno, T.; Kondoh, E.; Yamamoto, S.; Kikukawa, N.; Suemasu, T. Cu Coating Inside Small (15 μm) and Ultrahigh-Aspect-Ratio (> 130) Through-Holes Using Supercritical CO₂ Fluid. *Jpn. J. Appl. Phys.* **2014**, *53*, 05GA08.
- (36) Lee, J.-H.; Kim, Y.-S.; Constant, K.; Ho, K.-M. Woodpile Metallic Photonic Crystals Fabricated by Using Soft Lithography for Tailored Thermal Emission. *Adv. Mater.* **2007**, *19*, 791–794.
- (37) Li, W.; Zhou, Y.; Howell, I. R.; Gai, Y.; Naik, A. R.; Li, S.; Carter, K. R.; Watkins, J. J. Direct Imprinting of Scalable, High-Performance Woodpile Electrodes for Three-Dimensional Lithium-Ion Nanobatteries. *ACS Appl. Mater. Interfaces* **2018**, *10*, 5447.
- (38) Lee, J.-H.; Lee, J. C. W.; Leung, W.; Li, M.; Constant, K.; Chan, C. T.; Ho, K.-M. Polarization Engineering of Thermal Radiation Using Metallic Photonic Crystals. *Adv. Mater.* **2008**, *20*, 3244–3247.
- (39) Moridani, A. K.; Zando, R.; Xie, W.; Howell, I.; Watkins, J. J.; Lee, J.-H. Plasmonic Thermal Emitters for Dynamically Tunable Infrared Radiation. *Adv. Opt. Mater.* **2017**, *5*, 1600993.
- (40) Shan, X.; Schmidt, D. P.; Watkins, J. J. Study of Natural Convection in Supercritical CO₂ Cold Wall Reactors: Simulations and Experiments. *J. Supercrit. Fluids* **2007**, *40*, 84–92.
- (41) Oh, Y. S.; Choi, D. Y.; Sung, H. J. Direct Imprinting of Thermally Reduced Silver Nanoparticles via Deformation-Driven Ink Injection for High-Performance, Flexible Metal Grid Embedded Transparent Conductors. *RSC Adv.* **2015**, *5*, 64661–64668.
- (42) Barnes, W. L.; Preist, T. W.; Kitson, S. C.; Sambles, J. R. Physical Origin of Photonic Energy Gaps in the Propagation of Surface Plasmons on Gratings. *Phys. Rev. B: Condens. Matter Mater. Phys.* **1996**, *54*, 6227.
- (43) Barnes, W. L.; Dereux, A.; Ebbesen, T. W. Surface Plasmon Subwavelength Optics. *Nature* **2003**, *424*, 824–830.
- (44) Zayats, A. V.; Smolyaninov, I. I.; Maradudin, A. A. Nano-Optics of Surface Plasmon Polaritons. *Phys. Rep.* **2005**, *408*, 131–314.
- (45) Kreibig, U.; Vollmer, M. *Optical Properties of Metal Clusters*; Springer Science & Business Media, 2013.